

Optical plasma microelectronic devices

Ebrahim Forati^{1,*}, Shiva Piltan¹, Tyler J. Dill², Andrea R. Tao², and Dan Sievenpiper^{1,†}

¹ *Electrical and Computer Engineering Department,*

University of California San Diego, La Jolla, CA 92098 and

² *Department of NanoEngineering, University of California San Diego, La Jolla, CA 92098**

Abstract

The great majority of modern microelectronic devices rely on carriers within semiconductors due to their integrability. Therefore, the performance of these devices are limited due to natural semiconductor properties such band gap and electron velocity. Replacing the semiconductor channel in conventional microelectronic devices with a gas plasma channel may scale their speed, wavelength, and power beyond what is available today. However, gas plasma creation, without applying high voltages, is quite challenging in a practical device. Here, we successfully generate an electro-optically triggered gas plasma channel to be used in feasible microplasma devices. The combination of DC and laser-induced gas ionizations controls the conductivity of the channel, enabling us to realize different electronic devices such as transistors, switches, and modulators. A special micro-scale metasurface was used to enhance the laser-gas interaction, as well as combining it with DC ionization properly. Optical plasma devices benefit from the advantages of plasma/vacuum electronic devices while preserving most of the integrability of semiconductor-based devices.

* dsievenpiper@eng.ucsd.edu; forati@ieee.org

I. INTRODUCTION

In 1906, the first vacuum based electronic device, a diode, was invented by Fleming. Later, in 1907, Lee De Forest introduced the first vacuum based amplifier. Low pressure gas was then added to the vacuum tubes to increase their power handling due to the excess current generation by the ionized gas. During the 1960s and 1970s, gas-plasma electronic devices such as voltage regulators, switches, and modulators were widely used in RF communication and audio systems. After being mostly replaced by semiconductor counterparts, due to their integrability, gas-plasma devices (usually with micro-scale dimensions) were mostly studied for plasma displays, water treatment, ozone generation, pollution control, medical treatment, and material processing [1–4]. Semiconductors and gas plasma share the same mathematical framework. However, they are differentiated mainly by the identity of positive carriers (ions in plasma versus holes in semiconductors) and the existence of the periodic lattice in semiconductors. The advantage of gas-plasma lies in its higher mobility of electrons. As an example, the electron mobility under an electric field strength of 10^3 V/cm in neon gas (at pressure 100 Torr and temperature 300 K leading to the atomic density of $N_e = 3.2 \times 10^{18} \text{ cm}^{-3}$) is greater than $10^4 \text{ cm}^2 \text{ V}^{-1} \text{ s}^{-1}$. This mobility is ~ 7 times larger than the electron mobility in silicon (Si) at 300 K which is $\mu_m = 1350 \text{ cm}^2 \text{ V}^{-1} \text{ s}^{-1}$ [5, 6]. The higher mobility of an electron in gas plasma is mostly due to the lower number density of atoms (typically 4-6 orders of magnitude) compared to semiconductors. On the other hand, equilibrium electron number densities in doped semiconductors are typically in the 10^{15} – 10^{19} cm^{-3} range, achievable by microplasma devices as well. Microplasma devices are routinely capable of providing electron densities of 10^{16} cm^{-3} , and even peak electron density of $2 \times 10^{17} \text{ cm}^{-3}$ was reported in pulsed operation of an Al/Al_2O_3 device [7]. But, difficulties in plasma ignition/sustainment have been an obstacle in the design and application of practical microplasma devices. Two established methods of generating artificial plasmas are DC discharge, and laser-induced break-down (LIB), both of which have practical limitations [8]. In a DC discharge system, a gas is energized by applying high DC voltage between two conductive electrodes to create plasma while in a laser-induced plasma (LIP) system, the nonlinear interaction between a high power focused pulsed laser with the gas creates plasma [9–13]. The need for high DC voltages or high power laser intensities has been the limiting factor in microplasma device designs. In this work we successfully avoided

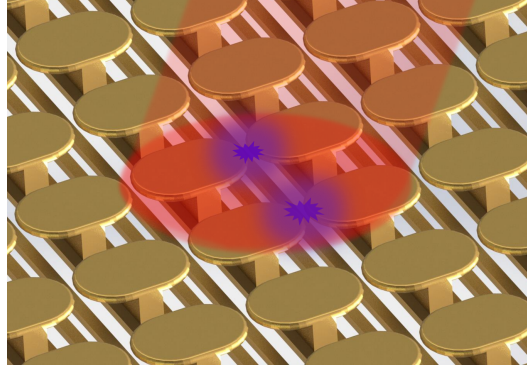


Figure 1. DC-biased resonant inclusions under illumination by a wavelength-tuned CW laser. Gas ionization initiates at the hot spots between the gaps, and eventually spreads over the entire surface.

these limitations by simultaneous photonic and electric excitation of the gas (combining DC and LIB ionizations). In order to preserve the integrability of our microplasma devices, we designed them on a silicon platform, aiming to create a link between the two different plasma genres: electron-hole and electron-ion. Devices with this link benefit from assets of both plasma/vacuum electronics (i.e. higher speed and power handling) and semiconductor electronics (i.e. the integrability).

A few groups have studied gas plasma near semiconductors to develop microplasma-based optoelectronic devices[1, 14–20]. These efforts mostly relate to the band structure of semiconductors, which bend due to the electric field presented in the plasma sheath in their vicinity. Therefore, neutralization of incoming ions by the semiconductor surface occurs simultaneously to the amplification of the electron field emission and secondary emissions by the biased semiconductor. The first microplasma device in Si was fabricated in 1997 by cylindrical micro-discharge cavities in Si, called hollow cathode discharge [21]. In a separate device, inverted square pyramids were filled with neon gas to make a photodetector [14]. Photoresistivity of 3.5 A/W was reported in the 420 – 1100 nm wavelength range. Recently, RF-fed microplasma has been considered for a lasing source using an optical pump [22]. As a closer example to our work, in [5], a plasma bipolar junction transistor (PBJT) was designed by replacing the semiconductor collector in a normal bipolar junction transistor (BJT) with gas plasma. While useful in specialty applications, the PBJT suffers from the plasma ignition problem (i.e., the collector in the designed PBJT required hundreds of volts

to ignite plasma and activate the PBJT). In our proposed scheme, by combining photonic-electric excitation of gas atoms, small DC voltages along with low power CW lasers can activate the device.

In order to increase the conductivity of plasma, we may leverage the resonant effect to liberate some electrons from inside a metallic structure and add them to plasma. In general, electrons can be freed from inside a metal by boosting their energies to exceed the surface voltage barrier of the metal, called the work function. Boosting electrons' energies can occur in different ways including thermally and by photon absorption, called the photoelectric event, discovered by Heinrich Hertz in 1887. [23]. Alternatively, the work function can be lowered using an external high intensity electric field at the metal surface, called the electron field emission, often explained by the Fowler-Nordheim theorem. Nonetheless, boosting electrons' energies and lowering the work function can occur simultaneously to liberate electrons using low energy photons. It has recently been shown that low energy photons coupled to surface plasmons can enhance and emit electrons with much higher energies than photons (i.e. plasmons decay into hot carriers) [24, 25]. In our scheme, a DC bias is applied to metallic resonant inclusions with excited surface plasmons. This may cause electron emission and/or ionize the surrounding gas directly. These emitted electrons can then accelerate due to the high electric field provided by the metasurface, and contribute to the three-body collision gas ionization mechanism. Figure 1 depicts the proposed plasma ignition technique in which plasma initiates at the high electric field spots between the resonant inclusions. This method allows us to control the degree of gas ionization both electrically (with DC bias) and optically (with the incoming laser). Existing research in plasma device arrays is limited to discrete devices, with no direct coupling of plasma or electric field between them. In our proposed concept, coupled cavities share a common gas volume, enabling the plasma to spread over a large area, and potentially allowing high power operation. Also, unlike our proposed concept, the optical properties of the existing microplasma device demonstrations come from absorption by a semiconductor, not through direct ignition of the plasma. We envision the use of our technique in designing different gas plasma-based devices with all the benefits of electron-ion plasmas such as high speed and high power handling.

In the following sections, the proposed concept and the metallic micro-structure surface are introduced in detail. Then, sample devices are discussed, demonstrating some of the opportunities that electron-ion plasma can provide.

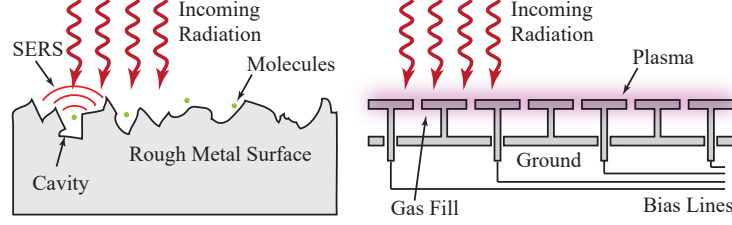


Figure 2. Inspired by SERS (left), the proposed concept is to initiate a plasma device using optical power pumping a designed resonant surface (right). The bias lines further reduce optical power requirements and provide photonic/electronic signal processing capabilities.

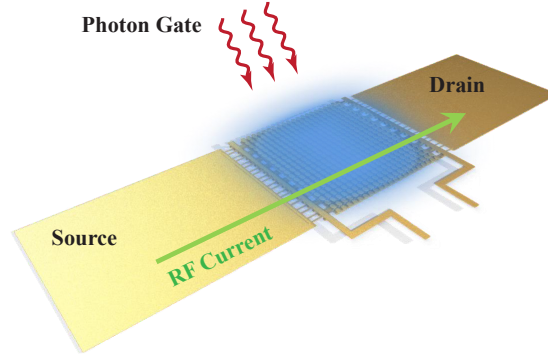


Figure 3. Photon-gate plasma transistor. The bias signal along with the incoming light intensity controls the conductivity between the source and drain.

II. THE PROPOSED CONCEPT

The design was inspired by surface-enhanced Raman scattering (SERS) in which the local electric field is greatly enhanced due to the surface roughness, as shown in Fig. 2, in order to amplify the Raman response of biomolecules [6, 26, 27]. The intention in the design of the device was to exploit the distributed high Q resonance, inherent in certain periodic structures, to dramatically enhance the absorption of local photons and build novel microplasma devices [28–30]. The resonant surface in Fig. 2 is immersed in argon (or any other inert) gas and is illuminated by a CW laser. The conductivity of plasma surrounding the periodic metallic structure is controlled by photonic and electrical signals. Besides

providing a high Q resonance, the surface enables DC excitation of the electrons in the metal and gas atoms. Existing microplasma devices typically contain the plasma within a “cavity,” but this is merely a vessel for confining the gas, not a resonant electromagnetic cavity. We propose to take advantage of the field enhancement provided by resonant coupled electromagnetic cavities to greatly enhance the response of the device to incoming radiation. The concept enables us to implement a range of new devices based on plasma rather than semiconductors. As an example, Fig. 3 shows a photon-gate plasma transistors in which source and drain electrodes are added to the resonant surface as shown in Fig. 3. When an incoming optical signal coincides with the surface resonance frequency, the result is substantial electric field enhancement across the gaps, igniting the plasma. As the plasma spreads across the surface, it forms a conducting path between source and drain. This is actually a four-terminal device (source, drain, bias, and photon-gate), and the conductivity between the source and drain is controlled by both the bias and the photon gate. The photon-gate provides complete electrical isolation, yet the surface is a highly scalable electron device, and therefore is potentially capable of handling high power. Thus, these devices could find applications as switches for microwave systems. They could also be used as photodetectors which can be tuned to any frequency by varying the geometry of the surface. It can even be designed so that different frequencies resonate with different regions of the surface, providing a highly sensitive yet broadband response. An optimized plasma transistor may also have advantages over semiconductor transistors. Since plasma is self-healing, events that would damage an ordinary semiconductor device (e.g. over-voltage or radiation) have little effect on a plasma device. Also, a plasma device may have many of the advantages of vacuum electron devices in that they can handle higher power levels at higher frequencies (this is why many high-power microwave amplifiers in use today are still traveling wave tubes). A plasma device is free from natural semiconductor properties such as the semiconductor band gap, which limits photon wavelength response, and electron velocity, which limits device speed. Because the performance of plasma devices depends on geometry, gas pressure, and other controllable parameters, they may offer greater flexibility in terms of broadband photodetectors or high speed transistors.

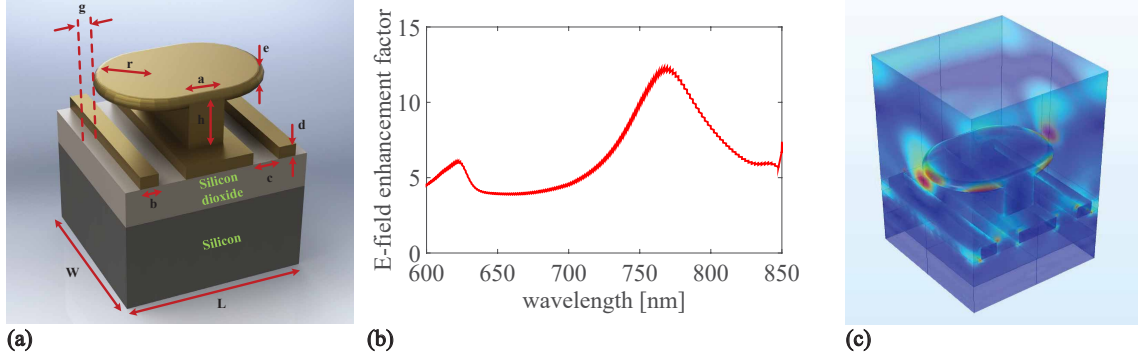


Figure 4. Unit cell of the resonant surface (a) and its full wave simulated electric field enhancement (b) and norm distribution (c). The dimensions are $a = 100, b = 100, c = 150, d = 80, e = 70, g = 50, r = 240, L = 850, W = 880$, all in nanometers. The field distribution is at $\lambda = 785 \text{ nm}$, and red color represents the highest value.

III. THE RESONANT SURFACE DESIGN AND DEVICES IMPLEMENTATION

Figure 4 shows the unit cell of the high Q resonant surface which we used to electro-optically initiate plasma. The unit cell consists of gold metallic inclusions, vertical gold posts topped with gold plates, on a silicon (Si) wafer with a layer of silicon dioxide (SiO₂) in between as isolation. Silicon wafers with a layer of SiO₂ (typically between 100 – 600 nm) are usually used as the substrate in photo-detection devices. The SiO₂ layer is used as an isolator to minimize the leakage current in the device. Usually a 200 nm thick layer of SiO₂ provides enough isolation. The Si wafers used in our experiments had 1000 Ωcm resistivity and the SiO₂ layer was coated on the wafer using plasma sputtering. Full wave simulation of the unit cell, as included in Fig. 4, confirms resonance at $\lambda = 785 \text{ nm}$ with the electric field enhancement of about $EF = 12$ under proper linear polarization (along the mushroom's length). The field enhancement is due to the localized surface plasmon resonance supported by gold [27, 31–35]. The resonant mode was optimized so that the enhanced electric field at resonance (hot spot) is confined to the gap between mushrooms. As a result, the maximum DC electric field (due to the bias), is superimposed with the laser-induced hot spot.

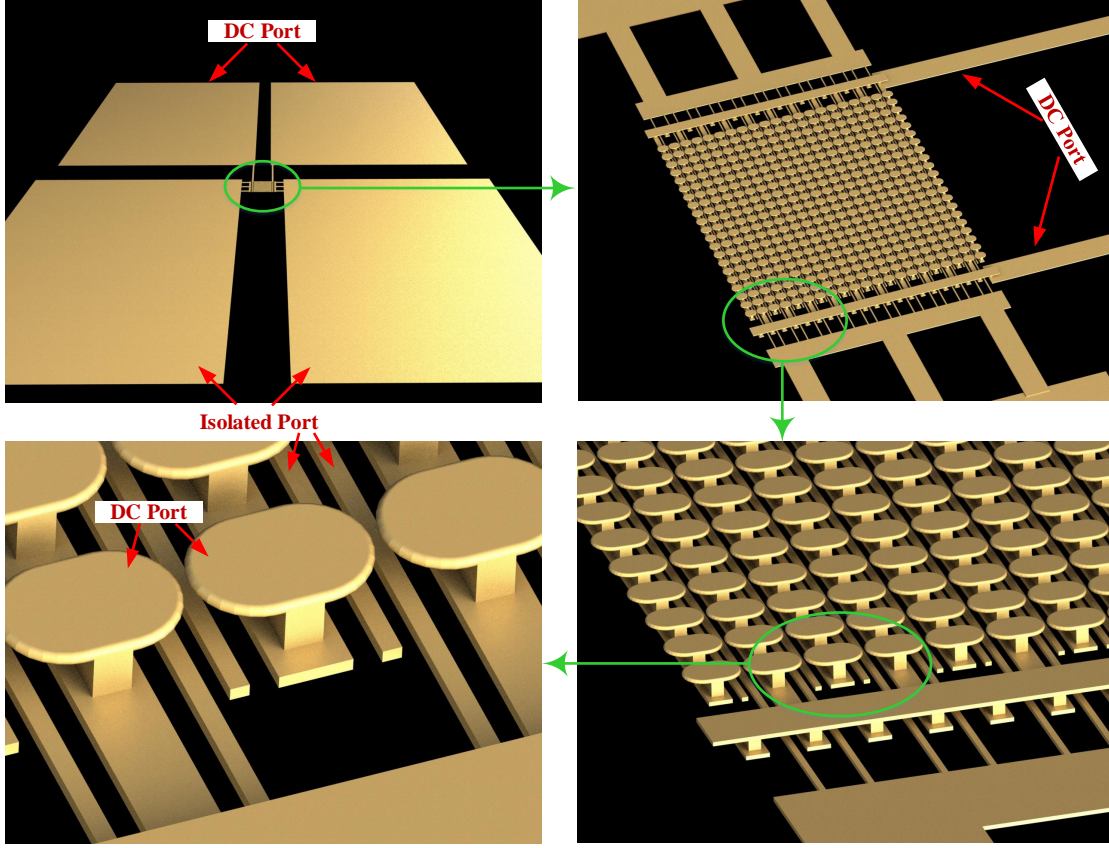


Figure 5. The designed optical plasma transistor. Mushroom rows are to be biased with alternating polarities, using the two airbridges on the sides, to form the DC port. The parallel strips on the substrate, below the gaps between the mushrooms, form the isolated port.

The unit cell in Fig. 4 also provides us two electrical ports. The DC electrical port consists of mushrooms, while the second electrical port is formed by the gold ribbons on the substrate, as shown in Fig. 4, and is called the isolated port. With this generic design, we verify two microplasma devices: a photon-gate transistor, and an optical switch, as will be discussed later. Figure 5 shows the final design including an array of 21 by 21 unit cells connected to four large square pads ($250 \mu m^2$) for wire-bonding. In order to form the DC port, so that the DC electric field hot spots lay inside the gap between the mushrooms, we needed to feed every other row of mushrooms with the same DC polarity. This was done by placing two air bridges on the surface sides, and connecting them to the wire bonding square pads, as clarified in Fig. 5. As a result, after biasing the DC port, adjacent mushroom rows will have opposite polarities. Similar to an inter-digital capacitor, the ribbons on the

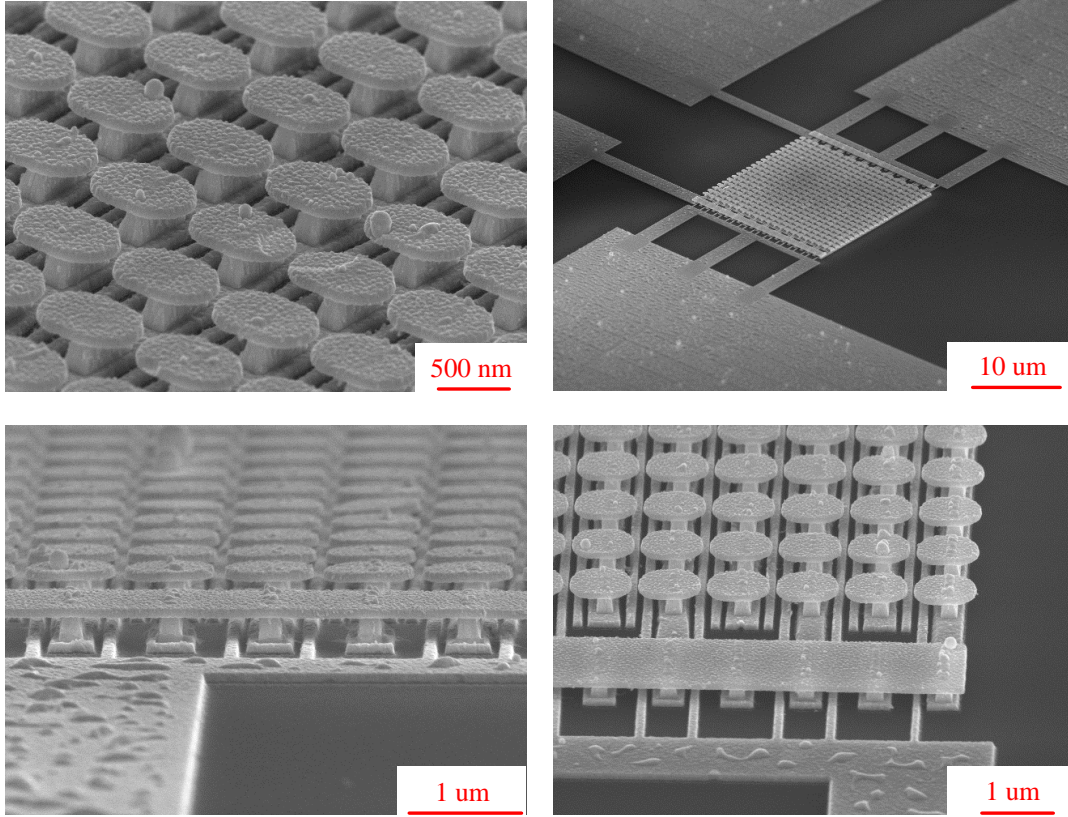


Figure 6. SEM pictures of the fabricated optical plasma transistor. The device is made of gold on Si substrate with a 180 nm thick SiO_2 layer as isolation.

substrate were also connected to the remaining two square pads, forming the isolated port. The surface was fabricated using a multi-step Ebeam lithography technique, as discussed in the methods section, and scattering electron microscopy (SEM) pictures of the surface and its air bridges are shown in Fig. 5.

In order to confirm the high Q resonance of the surface, four different fabricated samples were characterized using Raman spectroscopy. For each sample, the electric field enhancement factor was measured at 15 different locations. Their averages and standard deviations (percentage) are reported in Table 1. Details of the Raman spectroscopy and field enhancement determination is reported in the methods section. Based on the full-wave simulation results, the ratio of the maximum electric field (at the hot spot) to the average electric field on the surface (at resonance) is 1.24. Therefore, the maximum FE of surfaces can be approximated by multiplying the average FEs reported in Table 1 by a factor of 1.24. Based

on the results in Table 1, the average field enhancement of samples was around 30×1.24 . Obtaining very large enhancement factors is challenging due to metallic loss, as discussed in Refs. [36, 37]. To verify resonance, the FE of one of a sample was measured off resonance (at $\lambda = 633$ nm) which was almost half of the resonant FE, as reported in Table 1. This is consistent with the full wave simulation result, shown in Fig. 4 too. Reasons for observing higher experimental FEs than simulation results include surface roughness, chemical enhancement, and non-linearity of gold polarizability.

Sample #	$\lambda = 633$ nm FE_{ave}	$\lambda = 633$ nm SD	$\lambda = 785$ nm FE_{ave}	$\lambda = 785$ nm SD
1	-	-	30.5797048	1.0670
2	-	-	27.2645456	1.0561
3	-	-	29.3709024	1.1617
4	15.5295582	12.3933732	32.6136177	1.3008

The fabricated samples were then installed and wire bonded inside standard dual in-line packages, as shown in the supplemental materials (SM).

As the first example, an optical plasma switch was studied using the DC and the optical ports in Fig. 5. In the optical plasma switch, the optical port illumination varies the conductivity of the DC port sufficiently to realize ON and OFF states. The change in the conductivity is caused by gas ionization as well as possibly hot electron injection. Figure 7 shows the current versus voltage (I-V) curves of the DC port with and without the laser illumination at two different pressures. Throughout this paper, low pressure is 0.1 Torr and high pressure is 200 Torr. A tunable laser set at $\lambda = 785$ nm with a power density of 300 mW/mm^2 was used to illuminate the device. As Fig. 7 shows, with a DC bias of 5 volts, the conductivity of the dark device dramatically increases after laser illumination, which indeed is a switching behavior. The response of the optical plasma switch as a function of the laser power density and wavelength (under fixed bias voltages) are shown in Fig. 8. From Fig. 7, the dark conductivity of the device is slightly larger at high pressure (specially at higher bias voltages). This suggests that perhaps DC-driven gas ionization is the dominant mechanism, over electron emission, since there are more atoms available for ionization at higher pressures. On the other hand, unlike dark conductivity, the laser-illuminated conductivity of the device is higher at low pressure, based on Fig. 8. Electron

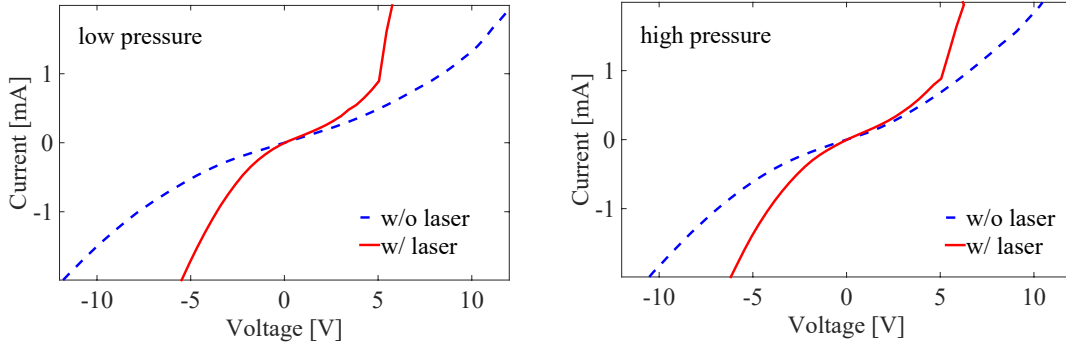


Figure 7. I-V curves of the DC port. The laser had $\lambda = 785 \text{ nm}$ and $S = 300 \text{ mW/mm}^2$. Low and high pressures are 0.1 mTorr and 200 Torr , respectively.

emission is generally stronger at lower pressures. Therefore, we suspect that the laser-driven electron emission (a.k.a. plasmon decay) is the dominant process in the device. The same conclusion can be made from the consistency between the wavelength dependence of the conductivity (shown in Fig. 8) and the laser electric field enhancement (shown in Fig. 4). More specific conclusions can be made regarding the contributions of electron emission and gas ionization by characterizing the device at high vacuum (on the order of 10^{-5} Torr), or by measuring the gas degree of ionization. In general, due to the similarity principle, the ionization per unit time (η) of gases is a function of the applied electric field (by DC bias or induced by a laser) and pressure as

$$\eta/p = f\left(E/p(1 + \omega^2\tau^2)^{1/2}\right), \quad (1)$$

in which E is the electric field (DC value or laser-induced rms value), ω is angular frequency, τ is the momentum transfer collision time, p is pressure, and f is a function which has been measured for many gases [38]. This function may be different in our scheme as both DC and laser induced electric fields present simultaneously.

As the second example, an optical plasma transistor (OPT), depicted in Fig. 3, was achieved by using both DC and isolated ports. Comparing to a bipolar junction transistor (BJT), the isolated and the DC ports in OPT are analogous to the collector-emitter, and the base-emitter ports in a BJT. In other words, the isolated port current can be controlled with the DC port (voltage/current). Moreover, the optical port can affect both the DC and the isolated port currents, which is an additional degree of freedom in designing OPT compared

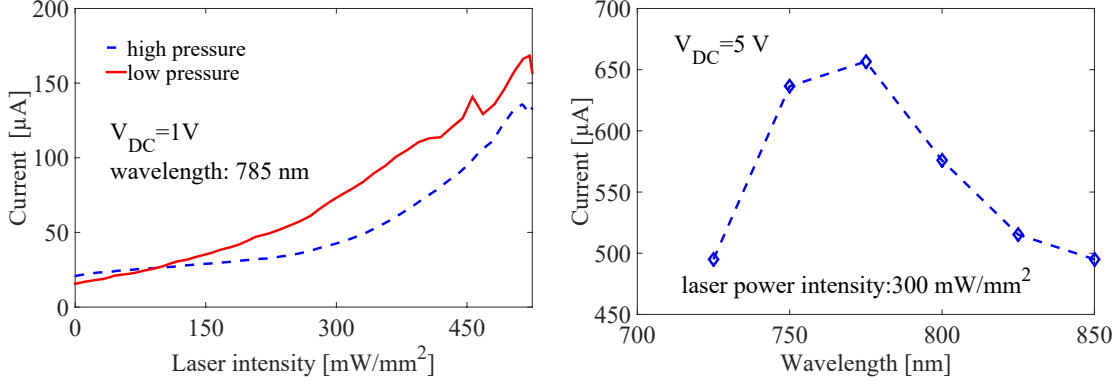


Figure 8. Responsivity of the DC port as a function of the laser power intensity (left) and wavelength (right). Low and high pressures are 0.1 *mTorr* and 200 *Torr*, respectively.

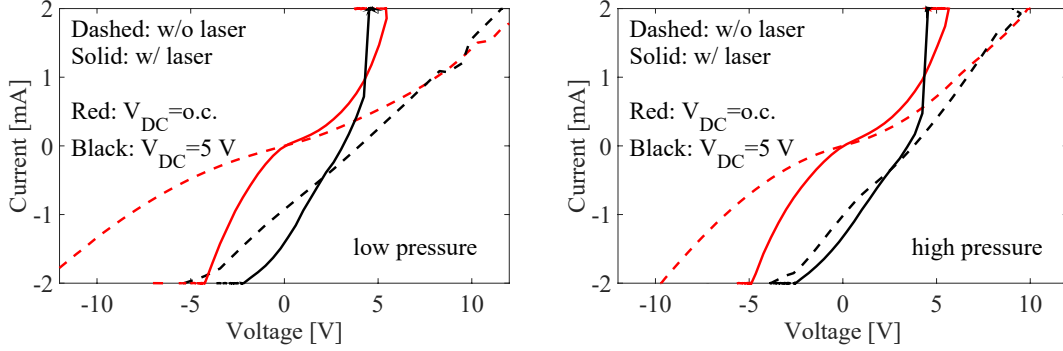


Figure 9. I-V curves of the isolated port under different DC port excitations. The laser had $\lambda = 785\text{ nm}$ and $S = 300\text{ mW/mm}^2$. Low and high pressures are 0.1 *mTorr* and 200 *Torr*, respectively.

to BJT. Figure 9 shows the I-V curves of the isolated port with different excitations of the DC and the optical ports.

Fig. 9 demonstrates successful control of the isolated port by both optical and DC ports, similar to a semiconductor transistor. The intense combined DC and AC electric field may liberate electrons from the conduction band of gold, and/or from the outer shell of Ar atoms [39]. In addition, liberated electrons (from any source) can accelerate in the induced electric field driving further gas ionization (through inverse Bremsstrahlung mechanism). In high vacuum, there are not enough Ar atoms for gas ionization and the electron field emission is the only existing mechanism. However, with the existing equipment, we are limited to 100 mTorr measurements.

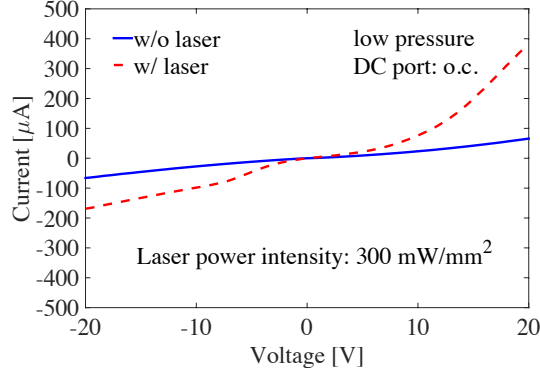


Figure 10. I-V curves of the square pads with and without laser illumination at pressure 0.1 *mTorr*.

The limited resistivity of the dark device is due to the leakage current through the sputtered SiO₂ layer and through the silicon substrate. Since the bandgap of silicon is smaller than the photon energy at $\lambda = 785$ nm, the laser also changes the conductivity of silicon. That is, some portion of the conductivity change in Fig. 9 is due to the silicon contribution. Also, the laser illumination and the plasma ignition cause a temperature change in Si and SiO₂, which leads to further conductivity change. We performed a few experiments to gather enough evidence that the gas ionization/field emission is involved. As the simplest experiment, the same I-V curves in Fig. 9 are measured by setting the illumination wavelength at $\lambda = 1050$ nm, at which photons were too weak for coupling to electrons in silicon. The results showed strong conductivity change. This was a strong evidence that silicon absorption was not the dominant mechanism at 785 nm either. As another experiment, the resonant surface was removed from the design, and a device was fabricated consisting of only the wire bonding square pads. Assuming that the pads are smooth enough to prevent SERS ionization, the only conductivity contribution in this device is silicon absorption and temperature rise. The I-V curves of this device are shown in Fig. 10, which indicate a smaller change in the conductivity compared to the OPT. As another experiment, several flat non-resonant devices were fabricated on glass substrate, as a good insulator, and none of them responded to the illuminating laser, as discussed in the SM.

IV. CONCLUSION

The concept of using combined low intensity DC and laser excitations to ignite plasma in argon was proved successfully. Two practical microplasma devices (optical switch and transistor) were successfully realized by a metallic micro-structure on Si substrate and were tested. After illuminating the DC biased device with laser, a conductive channel was created in the Ar gas via direct ionization of the gas atoms, and possibly electrons injection from the metal. The substrate in our design only supports the metallic structure and is not involved in the electric current flow. We anticipate that the concept will enable a wide range of new microplasma devices.

V. METHOD

A commercial finite element method code (HFSS) was used to simulate the unit cell, and Johnson-Christy model was adopted for gold. In order to simplify the simulations, mushrooms were set to have a smooth surface and rounded corners. This ensured that we avoided non-localities in the gold model and calculation singularities at the sharp corners [40]. As a result, the simulated field enhancement is a lower limit and, as will be shown later, the measured field enhancement will be larger. The measurement setup includes a tunable Ti:Sapphire laser pumped with a 10 W green semiconductor laser. The output laser beam was passed through two beam samplers for wavelength and power measurements. An Ocean optics spectrometer and a silicon photo-detector were used for wavelength and power measurements, respectively. The laser beam was sent into a vacuum chamber through a view port using a few optomechanics. The vacuum chamber was equipped with a vacuum pump, Ar gas inlet, pressure gauge, electrical feedthroughs, and a customized imaging system observing the device from outside of the chamber. The fabricated devices were installed in standard dual in-line packages with a small piece of carbon conductive tape (typically used in SEM) and wire bonded using a ball bonder. Two source-meters (Keithley 2400 and 2410) with a common ground were used for full characterization of the three port devices. In order to measure the I-V curves, the vacuum chamber was pumped down to 50 mTorr (our equipment limit) and then filled with Ar gas up to the desired pressure. The negative electrode of the two sourcemeters were connected to the optical table (ground), so two

terminals of the device’s ports were essentially connected.

A. Fabrication

A three-layers recipe was developed and optimized to perform the fabrication of clean mushrooms and air bridges. The first layer consisted of the gold ribbons on the substrate, the second layer included vias, and the third layer comprised the mushroom caps. After cleaning the wafer with acetone, 180 nm SiO₂ was deposited on the wafer using plasma sputtering. Then, the first layer was patterned and fabricated using Ebeam lithography and Ebeam evaporation (70 nm Au on top of 10 nm Cr as the adhesion layer). Similarly, the second layer (vias) was fabricated using Ebeam lithography and Ebeam evaporation (250 nm Au). In order to fabricate the third layer (mushroom caps), photoresist (AZ1505) was spin-coated on the sample and was ashed with oxygen plasma down to the thickness of 200 nm, so that the tip of the vias were exposed. Then, a few nanometers of chromium was sputter coated on the photoresist to prevent it from mixing with the Ebeam resist. Next, Ebeam resist was coated on the sample (without any soft baking) and was patterned using Ebeam lithography. The samples were then ready after metallization (70 nm Au), lift off using acetone, chromium plasma etching, and oxygen plasma cleaning.

B. Raman spectroscopy/ Experimental Determination of Field Enhancement

Experimental FEs were determined by comparing the enhanced spectra of thiophenol, a common SERS marker, to bulk Raman measurements and then dividing by the respective number of excited molecules. Because FE is dependent on $(E/E_0)^4$, we can approximate the average field enhancement over the device with this method.

Thiophenol forms a self-assembled monolayer (SAM) on gold surfaces. We performed an overnight thiophenol vapor phase deposition on the device. Excess thiophenol was removed by placing the device under vacuum for >2 hours. Raman measurements were conducted on both bulk thiophenol and on the thiophenol monolayer coating the gold surface of the device. Both sets of measurements were carried out using the same measurement configuration. All data was collected using either a 785 nm diode laser, or a 633 nm HeNe laser, at powers of < 1 mW, to ensure no desorption of the monolayer or morphological changes to the gold

structure. The FE was then calculated using

$$EF = \left(\frac{I_{\text{SERS}}}{I_{\text{Raman}}} \right) \left(\frac{N_{\text{Raman}}}{N_{\text{SERS}}} \right)$$

in which I is the measured bulk Raman or SERS Intensity, and N is the number of molecules from which the Raman signal originates. N_{Raman} was calculated using the density and molecular weight of bulk thiophenol along with laser focal volume. N_{SERS} was calculated from the gold structure area, multiplied by the literature packing value for thiophenol SAMs of 6.8 molecules/nm². The laser spot size was calculated using the scanning knife-edge method. The laser spot was scanned over a cleaved Si wafer edge in both X and Y directions and the 520 cm⁻¹ peak intensity was recorded over the length of the scan. The plots were fitted to error functions and the Gaussian beam waists derived. Focal Depth was calculated by translating the Si along the z-axis, with the focal plane in the center. This was fitted to a Gaussian and the focal depth was taken as the integral (-inf, inf) of the fit. Field enhancement was calculated using the 999 cm⁻¹ peak because it displays low orientational dependence on intensity, and is therefore less effected by molecular reordering on a metal surface. In addition it displays the highest bulk Raman signal and so gives us the most conservative FE calculation. Standard deviations were determined with measurements at >15 random points over the device surface.

ACKNOWLEDGEMENTS

The authors thank UC San Diego nanofabrication facility staff including Sean Parks, Larry Grissom, Ryan Anderson, Ivan Harris, and Xuekun Lu for the helpful discussions, and especially Maribel Montero for performing Ebeam lithography exposures.

FUNDING INFORMATION

This work was funded by Defense Advanced Research Projects Agency (DARPA) through grant N00014-13-1-0618.

AUTHOR CONTRIBUTIONS

Dan Sievenpiper proposed the idea and supervised the study. Ebrahim Forati conceived and conducted the fabrication and experiments. Tyler Dill performed and Andrea Tao supervised the Ramon spectroscopy measurements. Ebrahim Forati and Dan Sievenpiper analyzed the results. Ebrahim Forati wrote the manuscript. All authors reviewed the manuscript.

- [1] P. K. Singh, J. Hopwood, and S. Sonkusale, Scientific reports **4**, 5964 (2014).
- [2] A. P Papadakis, S. Rossides, and A. C Metaxas, The Open Applied Physics Journal **4**, 45 (2011).
- [3] R. Foest, M. Schmidt, and K. Becker, International Journal of Mass Spectrometry **248**, 87 (2006).
- [4] C. Tendero, C. Tixier, P. Tristant, J. Desmaison, and P. Leprince, Spectrochimica Acta Part B: Atomic Spectroscopy **61**, 2 (2006).
- [5] P. Tchertchian, C. Wagner, T. Houlahan, B. Li, D. Sievers, and J. Eden, Contributions to Plasma Physics **51**, 889 (2011).
- [6] L. V. Brown, K. Zhao, N. King, H. Sobhani, P. Nordlander, and N. J. Halas, Journal of the American Chemical Society **135**, 3688 (2013).
- [7] D. Yarmolich, Y. E. Krasik, E. Stambulchik, V. Bernshtam, J. Yoon, B. Herrera, S. Park, and J. Eden, Applied Physics Letters **94**, 011501 (2009).
- [8] S. C. Brown, *Basic data of plasma physics, 1966*, Vol. 1 (MIT Press Cambridge/Mass, 1967).
- [9] G. M. Weyl and D. Rosen, Physical Review A **31**, 2300 (1985).
- [10] M. Radmilović-Radjenović, B. Radjenović, M. Klas, and Š. Matejčik, Micro & Nano Letters **7**, 232 (2012).
- [11] F. Morgan, L. Evans, and C. G. Morgan, Journal of Physics D: Applied Physics **4**, 225 (1971).
- [12] C.-H. Chen, J. A. Yeh, and P.-J. Wang, Journal of Micromechanics and Microengineering **16**, 1366 (2006).
- [13] S. Brückner, W. Viöl, and S. Wieneke, “Coherence and ultrashort pulse laser emission,” (InTech, 2010) Chap. Interaction of Short Laser Pulses with Gases and Ionized Gases, pp.

- 383–403.
- [14] J. G. Eden, S. Park, N. Ostrom, and K. Chen, *Journal of Physics D: Applied Physics* **38**, 1644 (2005).
 - [15] W. Yuan, F. K. Chowdhury, and M. Tabib-Azar, in *Micro Electro Mechanical Systems (MEMS), 2012 IEEE 25th International Conference on* (IEEE, 2012) pp. 293–296.
 - [16] J. Eden, *Breakthroughs in Photonics 2010* **3**, 302 (2011).
 - [17] N. Ostrom and J. Eden, *Applied Physics Letters* **87**, 1101 (2005).
 - [18] K.-F. Chen and J. Eden, *Applied Physics Letters* **93**, 161501 (2008).
 - [19] Z.-H. Liang, H. Wang, H.-F. Liang, C.-L. Liu, and L.-G. Meng, *Plasma Science, IEEE Transactions on* **37**, 1782 (2009).
 - [20] C. Wagner, P. Tchertchian, and J. Eden, *Appl. Phys. Lett* **97**, 134102 (2010).
 - [21] J. W. Frame, D. Wheeler, T. DeTemple, and J. Eden, *Applied physics letters* **71**, 1165 (1997).
 - [22] W. Rawlins, K. Galbally-Kinney, S. Davis, A. Hoskinson, J. Hopwood, and M. Heaven, *Optics express* **23**, 4804 (2015).
 - [23] J. F. Mulligan, *Physics Today* **42**, 50 (2008).
 - [24] P. Dombi, A. Horl, P. Racz, I. Marton, A. Trugler, J. R. Krenn, and U. Hohenester, *Nano letters* **13**, 674 (2013).
 - [25] M. L. Brongersma, N. J. Halas, and P. Nordlander, *Nature nanotechnology* **10**, 25 (2015).
 - [26] M. Chirumamilla, A. Toma, A. Gopalakrishnan, G. Das, R. P. Zaccaria, R. Krahne, E. Rondanina, M. Leoncini, C. Liberale, F. De Angelis, *et al.*, *Advanced Materials* **26**, 2353 (2014).
 - [27] K. B. Crozier, W. Zhu, D. Wang, S. Lin, M. D. Best, and J. P. Camden, *Selected Topics in Quantum Electronics, IEEE Journal of* **20**, 152 (2014).
 - [28] D. Sievenpiper, L. Zhang, R. F. J. Broas, N. G. Alexopolous, and E. Yablonovitch, *Microwave Theory and Techniques, IEEE Transactions on* **47**, 2059 (1999).
 - [29] Q.-F. Yao, Y.-Z. Huang, J.-D. Lin, X.-M. Lv, L.-X. Zou, H. Long, Y.-D. Yang, and J.-L. Xiao, *Optics express* **21**, 2165 (2013).
 - [30] M. S. Eggleston, K. Messer, L. Zhang, E. Yablonovitch, and M. C. Wu, *Proceedings of the National Academy of Sciences* **112**, 1704 (2015).
 - [31] S. A. Maier, *Plasmonics: fundamentals and applications* (Springer Science & Business Media, 2007).
 - [32] S. A. Maier, *Optics Express* **14**, 1957 (2006).

- [33] S. A. Maier, Optical and quantum electronics **38**, 257 (2006).
- [34] J. Yao *et al.*, in *2009 Conference on Lasers and Electro-Optics and 2009 Conference on Quantum electronics and Laser Science Conference* (2009) pp. 1–2.
- [35] F. Wang and Y. R. Shen, Physical review letters **97**, 206806 (2006).
- [36] J. B. Khurgin, Nature nanotechnology **10**, 2 (2015).
- [37] P. R. West, S. Ishii, G. V. Naik, N. K. Emani, V. M. Shalaev, and A. Boltasseva, Laser & Photonics Reviews **4**, 795 (2010).
- [38] E. Yablonovitch, Applied Physics Letters **23**, 121 (1973).
- [39] H. F. Winters, in *Plasma Chemistry III* (Springer, 1980) pp. 69–125.
- [40] G. Toscano, S. Raza, S. Xiao, M. Wubs, A.-P. Jauho, S. I. Bozhevolnyi, and N. A. Mortensen, Optics letters **37**, 2538 (2012).
- [41] D. F. Sievenpiper, J. H. Schaffner, H. J. Song, R. Y. Loo, and G. Tangonan, Antennas and Propagation, IEEE Transactions on **51**, 2713 (2003).
- [42] H. Wakatsuchi, S. Kim, J. J. Rushton, and D. F. Sievenpiper, Applied Physics Letters **102**, 214103 (2013).
- [43] H. Wakatsuchi, S. Kim, J. J. Rushton, and D. F. Sievenpiper, Physical review letters **111**, 245501 (2013).
- [44] J. Butler, D. Goebel, R. Schumacher, J. Hyman, J. Santoru, R. Watkins, R. Harvey, F. Dolezal, R. Eisenhart, and A. Schneider, in *Microwave Symposium Digest, 1992., IEEE MTT-S International* (IEEE, 1992) pp. 511–514.

SUPPLEMENTAL MATERIALS

Figure 11 depicts the measurement setup. The fabricated devices were packaged (using standard dual in-line packages) and wire-bonded (using a ball bonder) as shown in Fig. 12,. Coaxial cables and connectors were used to feed the device inside the vacuum chamber. Use of coaxial cables prevented any plasma formation around the cables. The packages in Fig. 12 are ordered from Spectrum Semiconductor Materials Inc. (Part. no. CCF00604).

To confirm the significant effect of the resonant surface, some non-resonant structures (simple flat structures) were fabricated on quartz as shown in Fig. 13. The measured currents for all of these structures were less than 100 nA even with applied voltages above 100 V on either ports and with large laser illuminations greater than 1 W/mm^2 . Figure 14 shows a sample of current measurements using these devices. Quartz was chosen as the substrate for these flat structures to remove any possible substrate contributions in current measurements. We also tried to fabricate our resonant devices on quartz, but their fabrication was quite challenging since the pattern was too dense and the charge buildup on the isolator substrate distorted the Ebeam lithography repeatedly. Using conductive polymers as the charge dissipator layer did not solve the problem either.

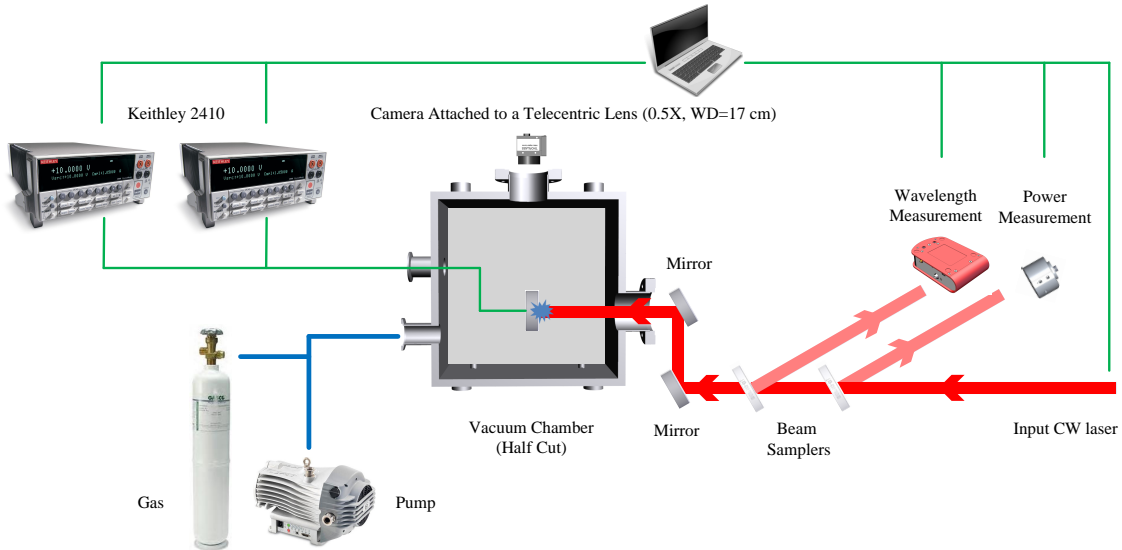


Figure 11. The measurement setup.

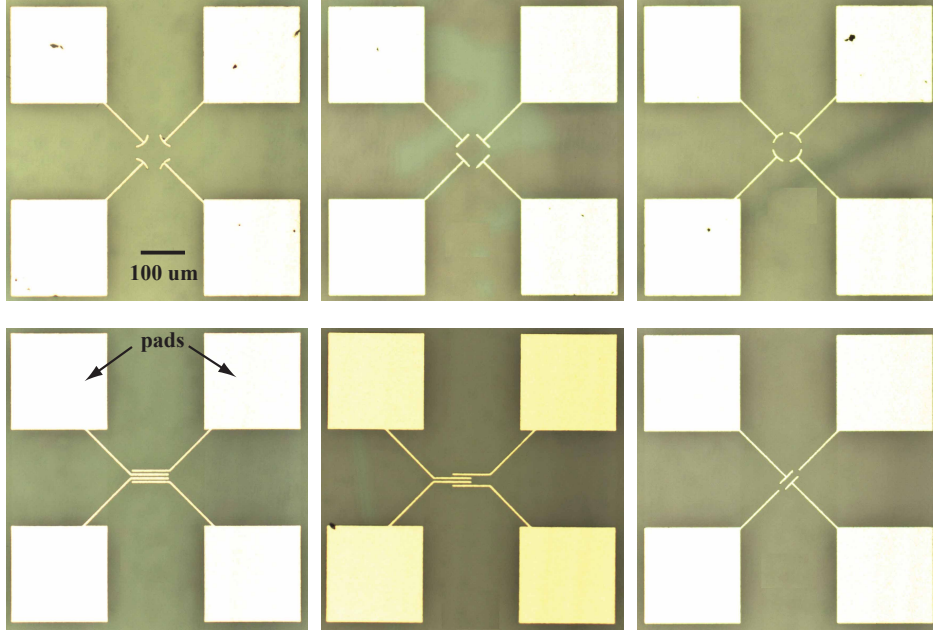


Figure 13. Fabricated non-resonant flat structures on quartz substrate.

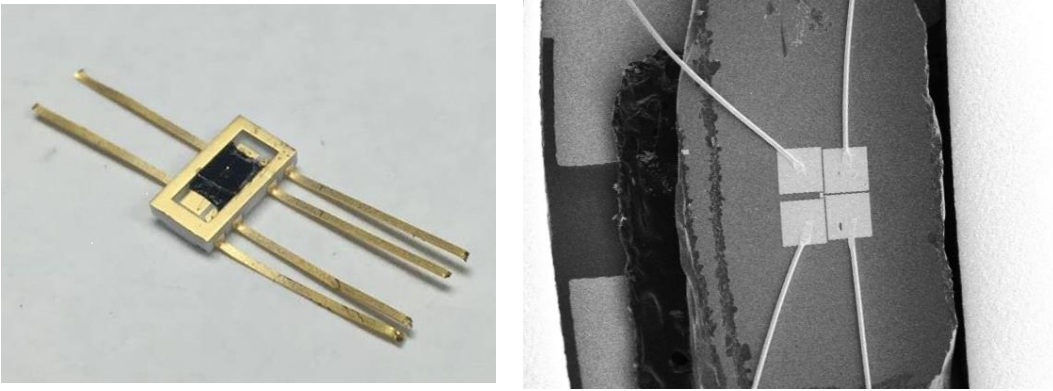


Figure 12. A device installed and wire-bonded in the package (left) and the SEM picture of the wirebonded device (right).

We anticipate that the proposed concept will enable a wide range of new devices such as photon-gate plasma transistors, active electromagnetic or photonic signal processing surfaces based on plasma effects, and plasma-based high-power sources for sub-mmW through THz frequencies as depicted in Fig. 15. Moreover, the designed surface cavities are electromagnetically coupled and share the same gas volume, so a small signal in one part of the surface

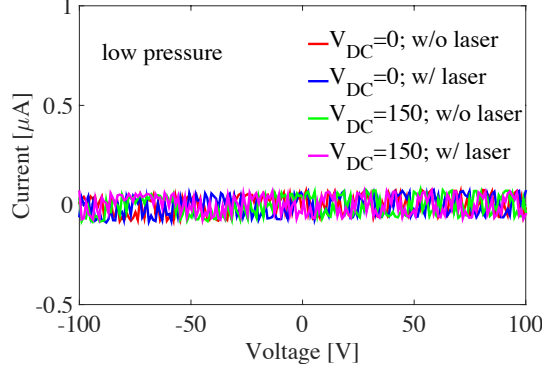


Figure 14. I-V curves of the non-resonant flat structures.

can ignite the entire array. This enables small RF or optical signals to modulate a large electric current, as envisioned in Fig. 15. An implementation of these resonant microplasma devices is for controlling the interaction between electromagnetic waves and surfaces, as illustrated in figure 15(b). This can include changing the surface impedance, reflectivity, and absorption properties. The reflection phase can also be varied across the surface to change the angle of reflection, such as a programmable grating. These structures have been built into steerable antennas at radio and microwave frequencies using semiconductor diodes, but the concept has not been extended to THz or optical frequencies [41]. Furthermore, nonlinear surfaces are currently under development for absorption of high-power microwave signals [42, 43]. Plasma surfaces can produce similar tuning or nonlinear effects, but can handle very high power compared to semiconductor-based structures. Furthermore, the use of plasma may enable these effects to be scaled beyond the frequencies available with solid-state diodes.

Another application is for high frequency amplifiers or sources, as illustrated in figure 15(c). Microscale tube amplifiers have been produced in the past, and our implementation may enable them to be scaled to higher power levels, and higher frequencies. For example, it is known that using plasma can improve the performance of vacuum electronics devices by preventing the electron beam from spreading, such as in the PASOTRON device (plasma-assisted slow-wave oscillator) [44]. This concept is also applicable to microplasma devices scaled to work at higher frequencies.

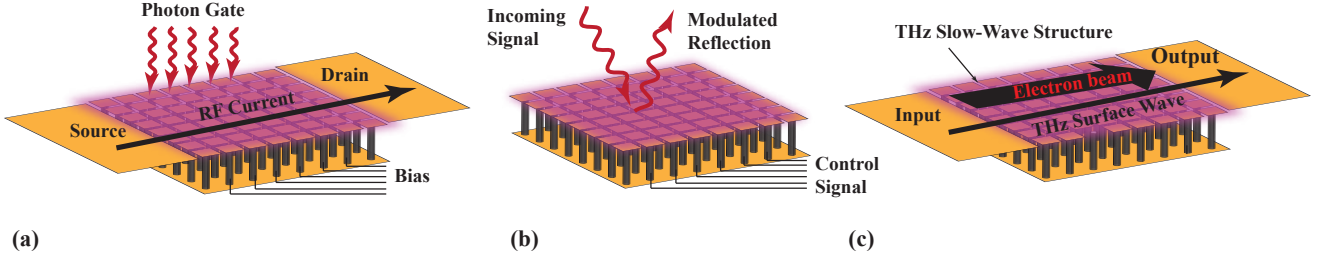


Figure 15. Notional metamaterial surface enhanced micro-scale plasma devices. a) Photon-gate transistor. The bias signal along with the incoming light intensity controls the conductivity between the source and drain. b) Optical signal modulator. The bias lines can be used to modulate the reflection or absorption properties of the surface. c) THz amplifier. Electrons are confined to the surface by plasma, and may be accelerated through several means, including the bias lines.